Title: A nucleation distance sets the cell size-dependent P-body assembly

Authors: Xuefang Gu[1], Dexin Shen[1], Xing Quan[1], Tatsuhisa Tsuboi[1,2,*]

Affiliations:

[1] Institute of Biopharmaceutical and Health Engineering, Tsinghua Shenzhen International Graduate School, Shenzhen 518055, China

[2] Tsinghua-SIGS & Jilin Fuyuan Guan Food Group Joint Research Center, Tsinghua Shenzhen International Graduate School, Shenzhen 518055, China

*To whom correspondence should be addressed:

Tatsuhisa Tsuboi

Institute of Biopharmaceutical and Health Engineering, Tsinghua Shenzhen International Graduate School, Shenzhen 518055, China

Tel: +86-152-1679-5216

E-mail address: ttsuboi@sz.tsinghua.edu.cn

Abstract:

Cells rely on various intracellular structures to regulate biological processes, including phase-separated granules. P-bodies are a type of membrane-less condensate found in eukaryotic cytoplasm that mediate mRNA degradation and storage. While the molecular composition of P-bodies is well studied, the relationship between their spatial organization and cell geometry, particularly cell size and organelle distribution, remains unclear. Here, we developed a conceptual framework to model phase-separation nucleation and validate the nucleation distance of a P-body in living yeast cells. Using microfluidic cell sorting and quantitative fluorescence microscopy, we found that smaller cells contain fewer, larger P-bodies, whereas larger cells form more, smaller granules. Monte Carlo simulations of P-body nucleation accurately recapitulate these cell size-dependent patterns, revealing a nucleation distance of approximately 2.2 µm. Furthermore, we demonstrate that increasing vacuolar volume reduces the effective cytoplasmic space and elevates the number of P-bodies, although cell size remains the dominant determinant. Our findings establish nucleation distance as a key parameter that links cell geometry to the biophysical regulation of condensate formation.

Keywords

P-body, cell size, phase separation, modeling, microfluidics

INTRODUCTION

Cellular structures act in concert to regulate essential processes such as intracellular transport, energy conversion, and gene expression [1–3]. Among these structures, membrane-less organelles formed through liquid-liquid phase separation (LLPS) play a critical role in gene expression regulation [4–6]. Cytoplasmic Processing bodies (P-bodies) are prototypical LLPS condensates in eukaryotic cells [3]. They sequester translationally repressed messenger RNAs (mRNAs) together with the decapping and decay enzymes [7,8], thereby orchestrating mRNA degradation, storage, and recycling [8–11]. P-body assembly involves several partially redundant scaffold proteins, including Edc3[12,13], Dcp2[14], Dhh1 [15], Pat1 [15,16], and Lsm4 [12,17], such that deletion of any one protein reduces P-body number and size and impairs the recruitment of client RNAs and proteins [18,19].

Phase separation begins with nucleation, the moment a small molecular cluster becomes large enough to overcome the energetic cost of forming a new interface. In supersaturated solutions or vapours, only molecules that diffuse within a reaction radius can bind productively; beyond this distance, collisions are too infrequent to surpass the nucleation barrier [20]. Once a condensate forms, it recruits nearby molecules, creating a depletion zone that reduces local supersaturation. New droplets can only nucleate beyond this depleted region. Together with the natural tendency of neighboring droplets to fuse and minimize surface energy, this phenomenon defines a characteristic nucleation distance (d_n), the typical spacing at which independent condensates can stably coexist [21]. Inside cells, molecular crowding and sub-diffusive dynamics further limit droplet fusion, allowing many condensates to persist at approximately d_n apart rather than merging into a single large phase[22]. Simulation using a coarse-grained protein model revealed that the stability of biomolecular condensates depends largely on the number of attractive interactions between

molecules[23]. By modulating concentration, crowding, or binding affinity, cells can tune d_n to control both the number and spatial distribution of condensates.

Despite the complexity of the intracellular environment, nucleation in living cells still adheres to fundamental physics constraints, the existence of an energy barrier, and the requirement for a critical molecular cluster, with cellular components often acting as seeds to facilitate this process [20]. The concept of a nucleation distance thus bridges physical theory and cell biology, as it arises from the necessity of accumulating sufficient molecules within a reaction radius and is reinforced by molecular depletion effects and coalescence dynamics, ultimately leading to a regulated, non-random spatial distribution of condensates within the cell. These insights suggest that P-body assembly is governed not only by protein composition and interactions but also by the physical dimensions and spatial organization of the cell.

Cellular organization is determined by the geometry of intracellular compartments and directly influences the scale and efficiency of biosynthetic processes [24–26]. As cells grow larger, organelles generally scale proportionally [27–29]. Although the total protein concentration is maintained, the concentration of individual proteins may increase or decrease with cell size [30–32]. Interestingly, P-bodies are known to appear during G1 and expand in size through G2, without a corresponding change in number [33], suggesting that spatial constraints, rather than protein abundance, may play a key role in phase separation. Yet, the precise influence of cell size and spatial parameters on P-body formation and dynamics remains largely unexplored.

82 Here, we extend this conceptual framework to quantitatively model condensate nucleation and
83 validate the presence of a characteristic nucleation distance in living cells. By combining
84 quantitative microscopy of size-sorted cells using microfluidic devices with Monte Carlo
85 simulations for nucleation, we find that larger cells tend to form more but smaller P-bodies,
86 whereas smaller cells generate fewer but larger P-bodies. The simulations identify a specific
87 nucleation distance (d_n) that aligns closely with our experimental observations. Moreover, in *sch9*Δ
88 and *vps1*Δ mutants, where vacuolar volume is enlarged and the effective cytoplasmic space
89 reduced, we observe a significant increase in P-body number, reinforcing the importance of spatial
90 restriction in Phase separation. Together, these results enable us to investigate how cells regulate
91 the nucleation distance to influence the formation, size, and distribution of phase-separated
92 compartments.
93

94 **Results**

95 **P-bodies number increases with increasing yeast cell size**

96 To examine the relationship between cell size and P-body formation under physiological
97 conditions, we set out to quantify how the spatial organization and cell geometry of a yeast cell
98 influence the initiation and abundance of P-bodies in vivo while avoiding genetic manipulations
99 that can secondarily perturb LLPS [34,35]. We developed a microfluidic device based on cell trapping
100 for long-period microscopy [36,37], machined with one hundred parallel trap lines whose constriction
101 widths gradually increase from 5.1 μm to 10 μm, enabling continuous perfusion of logarithmically
102 growing W303 cells and deterministic physical sorting by diameter (Fig. 1A, B, Supplementary
103 Fig. 1). This design provided a non-invasive and high-throughput method for examining a wide
104 range of cell sizes in a single experiment, while minimizing batch-to-batch variability

105 (Supplementary Fig. 1C). This platform preserved nutrient availability while imaging under an
106 identical glucose-starvation regime (0 % glucose, synthetic complete medium), a known
107 physiological condition that robustly induces P-body formation. The use of physical sorting rather
108 than genetic perturbation was crucial in isolating the impact of cell size per se, thereby avoiding
109 confounding effects such as stress responses, altered expression of phase-separation components,
110 or cell-cycle defects.
111
112 We tagged Dcp2, a core scaffold component of P-bodies, with a novel green fluorescent protein
113 variant, mAbbsinthe, which exhibits superior photostability and reduced aggregation relative to
114 commonly used GFPs (Supplementary Fig. 2A, B)[38]. Importantly, we confirmed that
115 Dcp2_mAbbsinthe retained P-body formation responsive to stress, validating it as a functional
116 reporter (Supplementary Fig. 2C). In addition, this choice was critical for long-term imaging of
117 condensate dynamics, especially under stress-induced conditions such as glucose starvation. Using
118 spinning-disk confocal microscopy, we captured three-dimensional image stacks of P-body
119 distribution in yeast cells of varying diameters (Fig. 1C). Quantitative analysis revealed a clear
120 positive correlation between cell size and the number of P-bodies (Fig. 1D). The mean P-body
121 number rose from 2.7 in 3.5–4.5 μm cells, 4.4 in 4.5-5.5 μm cells, to 6.2 μm in >5.5 μm cells.
122 These findings were corroborated using Edc3-GFP, an alternative P-body marker, validating that
123 the phenomenon is not tag-specific. Together, our results provide direct experimental evidence
124 that cell size is a determinant of P-body number, suggesting that physical cellular geometry plays
125 a role in influencing phase separation behavior.
126
127 **A Monte-Carlo simulation based on nucleation identifies a characteristic nucleation distance**

128 To test whether simple geometric constraints could explain the empirically observed scaling, we
129 implemented a Monte-Carlo simulation based on nucleation. In this model, we approximated the
130 yeast mother cell as a sphere and distributed virtual Dcp2 molecules randomly within its volume
131 (Fig. 2A). This abstraction was motivated by the physical properties of phase-separated
132 condensates, which behave as mesoscale entities with restricted mobility and volume-excluding
133 effects. Collisions resulting in center-to-center separations below a tunable threshold (nucleation
134 distance, d_n) trigger irreversible coalescence, conserving total mass. These fusion events were
135 iteratively calculated until all remaining molecular pairs were spaced beyond this threshold. We
136 initialized the model with 200 seed spheres per cell, each with radii ranging from 2.0 to 3.0 µm.
137 Across this range, a best-fit d_n of 2.2 µm simultaneously reproduced the monotonic increase in
138 punctum number with cell size (Fig. 1D, 2B, Supplementary Figure 3A). We then analyzed the
139 size of P-bodies. Since P-bodies were visualized through microscopy imaging, which potentially
140 results in deviations from their actual biological sizes. To ensure consistency between the
141 microscopy experiment and simulated data, we analyzed P-bodies size by calculating the
142 proportion of puncta in each size category. (Supplementary Figure 3B). We first matched the
143 category proportion between the two experiments for a cell size of 5.0 µm. With this size
144 classification, the simulation for the other two different size cells, 4.0 µm and 6.0 µm, matches
145 surprisingly well with the empirically observed triphasic size distribution of P-bodies (Fig. 2C -
146 G). Smaller cells tend to form larger P-bodies, whereas larger cells predominantly contain smaller
147 P-bodies. This agreement suggests that the physical spacing between successful nucleation events,
148 a feature not encoded in protein sequence or interaction affinity, acts as a central organizing
149 principle. To probe robustness, we performed sensitivity analyses varying initial molecular
150 numbers and cytoplasmic viscosity (Supplementary Figure 3C, D). The final puncta number was

151 largely invariant to particle count above ~200 and only weakly dependent on viscosity (within
152 biologically plausible ranges), indicating that d_n is the dominant determinant of condensate
153 distribution. These simulations highlight that spatial constraints and collision thresholds alone are
154 sufficient to explain the observed morphological transitions, without invoking complex
155 biochemical regulation.
156

157 **Organelle occupancy amplifies nucleation frequency by restricting effective cytoplasmic**
158 **volume**

159 While total cell volume increases during growth, the effective cytoplasmic space available for P-
160 body formation may be limited by the presence of large organelles such as the vacuole and nucleus.
161 To explore the impact of such intracellular crowding, we extended our simulation to incorporate
162 internal organelles occupying specific volumetric fractions. We implemented three distinct models
163 to simulate molecule fusion paths in the presence of a central spherical nucleus and vacuole,
164 representing non-permissive organelle space: (1) path-restricted fusion where molecular lines
165 crossing the nucleus were invalid, (2) path-shifted fusion where granules repositioned to avoid
166 organelle overlap, and (3) path-redirected fusion where particles navigated around obstacles using
167 a calculated shortest path (Fig. 3A–C).
168 Across all models, increasing organelle volume fractions consistently led to elevated final P-body
169 counts, even under a constant nucleation distance (Fig. 3D–G). This effect arose because internal
170 obstructions constrained the diffusion space, increasing local molecule concentrations and
171 reducing the effective reaction volume. These simulations suggest that intracellular crowding can
172 enhance condensate nucleation independent of changes in protein concentration or binding

173 affinity, highlighting a potential mechanism for tuning granule formation through organelle scaling
174 or spatial reorganization.
175
176 **Vacuole mutants validate the influence of spatial confinement on P-body assembly**
177 To test the simulation-derived hypothesis that intracellular crowding promotes condensate
178 nucleation, we examined two yeast mutants known to affect vacuolar morphology: *sch9*Δ and
179 *vps1*Δ. Both mutations are known to increase vacuole-to-cell volume ratios through distinct
180 mechanisms: *vps1*Δ via impaired membrane fission and *sch9*Δ via defects in nutrient sensing and
181 vacuolar growth regulation[27,39]. Quantification of vacuole-to-cell volume ratios confirmed
182 significantly increased organelle occupancy in both mutants compared to wild-type (Fig. 4A, B).
183 Fluorescence intensity analysis showed that Dcp2_mabbsinthe expression remained unchanged
184 (Fig. 4C), ensuring that any observed effects on P-bodies were not due to altered protein abundance.
185 As predicted by the simulation, *vps1*Δ cells exhibited significantly higher P-body counts across all
186 size bins (Fig. 4D), indicating that reduced cytoplasmic space can elevate nucleation rates.
187 Surprisingly, *sch9*Δ cells, despite also showing increased vacuole volume, did not exhibit a similar
188 rise in P-body number. Instead, both *sch9*Δ and *vps1*Δ displayed a marked shift toward smaller P-
189 body sizes (Fig. 4E, F), especially in larger cells.
190 This discrepancy can be reconciled by considering the nonlinear relationship between volume and
191 linear distance: a 10% reduction in cytoplasmic volume translates to only a ~0.17 µm. For details,
192 a 10% reduction in volume leads to only about 3.45% shrinkage in radius, which, for typical yeast
193 cytoplasmic dimensions (~5 µm), results in a 0.17 µm decrease in distance. Reduction in effective
194 radius, which is minor compared to the ~2.2 µm nucleation distance inferred from simulations.
195 Thus, small changes in cytoplasmic diameter may be insufficient to affect nucleation probability

196 but may still impair granule coalescence, favoring fragmentation in *sch9*Δ cells. In addition, the
197 simulated puncta numbers correspond to when the central sphere is calculated with less than 1%
198 of whole cell volume, using a d_n of 2.2 μm, which is far below the actual occupation by the
199 organelles (Fig. 3D-F). This suggests that effective intervention by the cellular organization must
200 be much smaller, possibly due to the condensate itself, which diffuses within the cell. These
201 findings experimentally confirm that intracellular crowding affects P-body morphology and
202 support the existence of a spatially constrained fusion threshold that governs the organization of
203 condensates.
204
205 **Larger P-bodies exhibit delayed disassembly upon nutrient repletion**
206 Having established that spatial parameters regulate condensate number and size, we next asked
207 whether these morphological features influence functional stability. In classical phase-separation
208 systems, larger droplets are thermodynamically favored and dissolve more slowly due to reduced
209 surface-to-volume ratios and kinetic buffering [40]. We hypothesized that large P-bodies would
210 persist longer upon glucose reintroduction, providing a functional correlate to their size. We
211 performed time-lapse confocal imaging of glucose-starved cells subjected to nutrient repletion and
212 tracked P-body disassembly over a 10-minute window. As expected, small and medium P-bodies
213 disappeared rapidly, with >80% disassembling within 4 minutes (Fig. 5A–B). In contrast, large P-
214 bodies were highly stable, often persisting until the final time point. This size-dependent
215 disassembly rate suggests that larger condensates have altered material properties, such as
216 increased viscosity or reduced surface curvature, that slow their dissolution. These results suggest
217 that condensate size is not merely a geometric consequence of fusion events but has functional
218 implications for granule stability and cellular memory. Larger P-bodies may act as more robust

219 repositories for mRNA and protein complexes, potentially influencing translational reactivation or
220 RNA decay following stress relief. This observation supports a model in which P-body size
221 encodes distinct biophysical states, governed by nucleation and fusion history, and modulated by
222 spatial constraints during formation.
223

224 **Discussion**

225 Our quantitative imaging combined with microfluidic cell size sorting and Monte Carlo modeling
226 shows that phase-separated P-bodies follow a characteristic nucleation distance (~2.2 μm), which
227 affects their number based on the overall cell diameter (Fig. 1, 2). By demonstrating that a single
228 geometric parameter is sufficient to recapitulate the full empirical relationship between cell size
229 and condensate number, we provide, to our knowledge, the first *in vivo* measurement of a
230 nucleation distance for any biomolecular condensate. This finding confirms long-standing
231 predictions from classical nucleation theory [20–23] and extends them to the crowded, heterogeneous
232 cytoplasm. Previous work has shown that many organelles scale with growth [24–29], but whether
233 equivalent principles govern LLPS compartments has been unclear. Our microfluidic approach
234 allowed us to modulate cell diameter without genetic perturbation or cell cycle arrest, cleanly
235 separating geometrical from biochemical variables. The experiments showed larger cells
236 consistently accumulated more, but smaller, P-bodies (Fig. 1D). The simulation showed that this
237 pattern naturally forms when nucleation events are prevented within d_n of an existing droplet: as
238 the cytoplasmic volume increases, the number of non-overlapping spheres of radius d_n roughly
239 increases with volume (Fig. 2A-C). These data argue that cells can modulate condensate
240 abundance passively, simply by growing. Our minimal model deliberately omits molecular
241 interactions, active transport, or cytoskeletal barriers, yet captures the essential statistics of P-body

242 distribution. This parsimonious view suggests that d_n signifies a fundamental effective reaction
243 radius that incorporates all microscopic determinants (multivalent interactions, crowding,
244 diffusivity) into a single mesoscale parameter. Future work can refine this framework by allowing
245 d_n to vary in response to environmental cues, post-translational modifications, or ATP levels,
246 ultimately enabling the quantitative prediction of condensate patterns from first principles.
247
248 Extending the model to include a central vacuole and nucleus showed that increasing internal
249 occupancy raises condensate number even at constant cell size (Fig. 3). The effect is conceptually
250 similar to the soft wall confinement used to promote vapour nucleation in microfluidic cavitation
251 chambers: reducing accessible volume raises the local supersaturation of phase separating
252 components and shortens the mean free path required to exceed the nucleation barrier. The vacuole
253 enlarged mutant *vps1*Δ validated this prediction in vivo, exhibiting higher P-body counts across
254 all size bins (Fig. 4D). By contrast, *sch9*Δ increased vacuole volume but did not change granule
255 number, highlighting that modest reductions in linear distance (< 0.1 μm) are negligible relative to
256 d_n, yet still fragment larger condensates and bias the population towards smaller droplets (Fig. 4E–
257 F). Together, these observations position spatial confinement as a tunable knob for condensate
258 biogenesis, complementing known biochemical regulators such as post translational modifications
259 or RNA scaffolding [9–12,14–18,41].
260
261 The strikingly slower dissolution of large P-bodies after glucose re-addition (Fig. 5) mirrors classic
262 Ostwald ripening behaviour, in which surface curvature drives exchange with the soluble pool.
263 Our data, therefore, suggest that the history of nucleation and fusion events leaves a lasting
264 physical imprint that regulates the lifetime of stress-induced mRNA repositories. A speculative

265 but attractive model is that large, stable granules favour selective retention of particular mRNAs
266 or protein complexes, endowing cells with a tunable memory of past stress episodes. P-bodies are
267 known to appear in G1 and grow through G2 without changing in number [33]. We reconcile this
268 observation with our findings by noting that budding yeast double their diameter only late in the
269 cell cycle; before this size threshold is crossed, the cytoplasm remains too small to permit
270 additional nucleation sites. More broadly, any physiological or pathological state that alters cell
271 volume or organelle allotment, such as hypertrophic growth, vacuolar fragmentation in aging, or
272 lysosomal enlargement in neurodegeneration, could reshuffle the cellular condensate landscape.
273 Indeed, impaired clearance of RNA granules is implicated in ALS and related disorders [6]. We
274 propose that disrupted spatial scaling, rather than intrinsic changes in phase-separating proteins,
275 may contribute to the aberrant accumulation of condensates in these contexts.
276
277 We imposed glucose starvation to synchronize P-body formation; whether d_n is conserved for other
278 stresses or constitutive granules, such as stress granules, remains to be tested. Additionally, the
279 model treats cells as perfect spheres and neglects the geometry of buds or cytosolic viscosity
280 gradients. High-speed light sheet imaging of nascent granules could capture the accurate
281 nucleation kinetics and refine these assumptions. Furthermore, our static snapshots cannot
282 distinguish between *de novo* nucleation and the fission of pre-existing droplets; combining
283 selective photoconversion with long-term tracking would resolve this issue. Finally, although we
284 focused on scaffold protein concentration, RNA itself can nucleate P-bodies [41]; incorporating
285 measured RNA fluxes may sharpen model accuracy. By quantitatively bridging cell-scale
286 geometry with mesoscale phase behaviour, our study uncovers a simple spatial rule that governs
287 how many condensates a cell can host. We anticipate that nucleation distance will prove to be a

288 unifying concept across diverse LLPS assemblies, offering a geometric lens through which to
289 interpret the dynamic self-organisation of the cytoplasm.
290
291 **Methods**
292 **Yeast strains and plasmids**
293 The yeast strains and plasmids used are listed in Supplementary File 1, and the oligonucleotides
294 used for plasmid construction and gene modification are listed in Supplementary File 2. To reduce
295 variability among the constructed yeast strains, the strains were created either through the
296 integration of a linear PCR product or a plasmid linearized through restriction digestion. The
297 variants of yeast expression plasmids (TTP257, PXQP017, PXQP032) for fluorescent protein were
298 constructed by swapping GFP of pFA6a-link-yoGFP-SpHis5 [42]with mAbb0.5 and mAbbsinthe[38]
299 through the combination of Gibson assembly and PCR. Fluorescent protein tagging for Dcp2 and
300 Edc3 with mAbb0.5, mAbbsinthe, and yoGFP was performed with PCR-mediated homologous
301 recombination using pFA6a-link-mAbb0.5-SpHis5, pFA6a-link- mAbbsinthe-SpHis5, and
302 pFA6a-link-yoGFP-SpHis5, and integrations were confirmed by microscopy. Su9-mCherry was
303 expressed by the TDH3 promoter from the integrated plasmid TTP076, and the strains with three
304 copies of the integrated plasmids in a cell were screened through microscopy and used for further
305 experiments. Deletion mutant strains were constructed with PCR-mediated homologous
306 recombination using pFA6a-hphMX6, and the integration of the hphMX6 cassette was confirmed
307 by PCR followed by electrophoresis.
308
309
310

311 **Microfluidic device fabrication**

312 The design and fabrication of the microfluidic device for yeast replicative aging were based on
313 previously published work [43,44]. To enable the capture of yeast cells with different diameters, the
314 initial 6 µm cell trap design was adjusted to include trap diameters ranging from 5.1 to 10 µm.

315

316 **Setting up a microfluidic experiment**

317 Before the microfluidics experiment, the device was placed under vacuum for 20 minutes to
318 remove air from the channels. The device was then placed on the stage of an inverted spinning
319 disk confocal microscope. Media ports were connected to plastic tubing, which in turn was
320 connected to 20 mL syringes filled with fresh synthetic complete medium (SD) (CSM powder
321 from Sunrise Science, #1001-100, supplemented with 2% glucose and 0.04% Tween-20). These
322 syringes were positioned approximately 24 inches above the microscope stage to drive media flow
323 via gravity. The waste port was connected to tubing positioned at stage height to maintain a stable
324 flow of waste.

325 Yeast cells were grown in 3 mL of SC medium and cultured overnight at 30°C to an OD_{600} of more
326 than 1.0. For loading, cells were diluted to an OD_{600} of 0.1 and cultured for 4 or 5 hours to an OD_{600}
327 of 0.5-0.7. The media syringe was replaced with the syringe containing the yeast culture
328 temporarily for loading cells. Most traps were filled within 1 to 2 minutes. Medium flow into the
329 device was gravity-driven, allowing cells to enter and occupy the traps. Most traps were filled
330 within 1 to 2 minutes. After loading, the yeast culture syringe was replaced with the media supply
331 syringe, and all tubing heights were adjusted to maintain a height differential of approximately 60
332 inches.

333

334 **Microscopy**

335 A P-body visualization experiment in a 96-well plate was performed as follows: Yeast cells were
336 grown in SC medium with 2% glucose in a 12 mL tube at 30°C with a rotator speed of 70 rpm.
337 100µl of mid-log phase yeast cells (OD600 of 0.4 to 0.7) were harvested and placed into a 96-well
338 Glass Bottom Plate (Cellvis LLC) coated with 0.1 mg/mL concanavalin A (Sigma-Aldrich C2010).
339 After 15 minutes of incubation, the well was washed twice with 100 µL of SC media without
340 glucose and then filled with 100 µL of SC media without glucose.

341 Image data for visualizing P-bodies in a microfluidic device were collected as follows: Yeast cells
342 were grown in SC medium using a 15ml glass tube at 30℃ with a rotator speed of 70 rpm until
343 they reached an OD_{600} of approximately 1.0. The following day, yeast cells were diluted to an
344 OD_{600} of 0.1 and cultured for an additional 4 to 5 hours until they reached an OD_{600} of
345 approximately 0.6, before being used in the experiment. To capture the cells in the microfluidic
346 device, the culture was diluted 4-fold and transferred into a 20 mL syringe prefilled with fresh SC
347 medium containing 0.04% Tween-20. After loading into microfluidics chips and 30 minutes of
348 glucose starvation, an image was collected.

349 Microscopy: Cells were imaged at 23℃ by an Eclipse Ti2-E Spinning Disk Confocal with
350 Yokogawa CSU-X1 (Yokogawa) with 50 µm pinholes, located at the Tsinghua-SIGS Tsuboi
351 Laboratory. Imaging was performed using a CFI Plan Apochromat Lambda 100x 1.49 NA oil
352 objective. Z-stacks (300nm steps) were acquired by a Prime 95B sCMOS camera (Photometrics)
353 (pixel size 0.11µm). Imaging was controlled using NIS-Elements software (Nikon). Images of the
354 microfluidic device were acquired using the large-image acquisition mode. The scanning area was
355 set to 0.1 × 1.5 mm with a 10% overlap between adjacent fields.

356

357 **The measurement of the photobleach resistance**

358 To measure the photo bleach resistance of GFPs, a 488 nm laser, and a 510–520 nm emission filter
359 were used. The cells were imaged with 50% of pre-set laser power 20 times. 25 flames of z-section
360 with 100 milliseconds were acquired in steps of 300nm. After background subtraction, the total
361 fluorescence intensity was divided by the cell occupation area in the image. The fluorescence
362 intensity was normalized to the initial intensity to obtain Relative Fluorescence Strength (RFS).
363 The average RFS of the 30 cells was calculated, and the RFS curve was created by MATLAB
364 (version 2021a) using polynomial curve fitting.

365

366 **Molecular nucleation model for P-body formation**

367 The model was based on Monte Carlo simulation approach. Since the yeast cell is approximately
368 spherical, it was modeled as a spherical region in the simulation. P-bodies are randomly distributed
369 in the cytoplasm and are also roughly spherical; therefore, in the simulation, they were also defined
370 as spherical molecules. Details were as followed:

371

372 First, the initial number of molecules per cell and the number of simulated cells were defined. Cell
373 diameter was used to represent different cell sizes. In each simulation, the initial position and
374 volume of each molecule were assigned using a random number generator, and their positions
375 were marked in a three-dimensional Cartesian coordinate system. The following procedure was
376 employed to generate the three-dimensional coordinates for each molecule:

377 (1) Random angle generation: Two angles, θ and φ, representing the azimuthal and polar angles in
378 spherical coordinates, were generated using uniform random distributions.

379 (2) Radial distribution: A radial coordinate was calculated based on the predefined cell radius, with
380 a cube root distribution applied to ensure uniform volume distribution.
381 (3) Position conversion: Using the standard spherical-to-Cartesian coordinate transformation, the
382 position in spherical coordinates was converted to three-dimensional Cartesian coordinates
383 according to the following equations:

384 $$x = r * cos(\theta) * sin\,(\varphi)$$

385 $$y = r * sin(\theta) * sin\,(\varphi)$$

386 $$z = r * cos\,(\varphi)$$

387 Since this study induced P-body formation by applying glucose starvation stress, the mobility of
388 P-bodies in this condition is very slow and can be neglected [45]; therefore, molecules were
389 considered to be in a static state. When the distance between two molecules fell below a critical
390 threshold (a predefined nucleation distance), these molecules were assumed to aggregate to
391 become one molecule.
392
393 The aggregation process was implemented as follows:
394 (1) Distance calculation and collision detection: To efficiently identify the closest pair of
395 molecules, an auxiliary function, findclosestpoint, was developed. Different models use different
396 findclosestpoint functions, as mentioned in Figure 3.
397 (2) Molecule merging: Upon collision, the volumes and positions of the two molecules were
398 merged. The resulting molecule had an increased volume, and its position was determined by
399 findclosestpoint.
400 (3) State update: The number and positions of molecules in the cell were updated accordingly after
401 each aggregation event.

402 The code updated the distribution of molecules in the cell based on the current positions and
403 volumes at each simulation step, progressively approaching the final aggregation state. The
404 simulation loop was terminated once the distances between all molecules exceeded the predefined
405 nucleation distance.
406
407 **Quantification and statistical analysis**
408 Detailed statistics, including the number of cells analyzed, mean value, standard deviation, and
409 standard error of the mean, are indicated in each figure legend. The Wilcoxon rank-sum test was
410 performed using GraphPad Prism (GraphPad software).
411
412 **Data and materials availability**
413 All data supporting the findings of this study are available within the paper and its supplementary
414 information. Yeast strains and plasmids used in the study are provided in Supplementary File 1.
415 The oligonucleotides used are listed in Supplementary File 2. Further information and requests for
416 raw data and reagents should be directed to and will be fulfilled by the lead contact, T.T.
417 (ttsuboi@sz.tsinghua.edu.cn).
418
419 **Code Availability**
420 The Pytorch codes for p-body drug screening can be found at
421 https://github.com/xuexuegu/nucleation.git.
422
423 **Supplemental information**
424 **Supplementary File 1 | List of oligonucleotides used for yeast construction**
425

Acknowledgments

We thank Nathan Shaner and Gerard Lambert for sharing mAbb0.5 and mAbbsinthe plasmids. We thank Abdul Khan for his helpful discussions and feedback on the paper. This work was supported in part by the Key Research and Development Program of the Ministry of Science and Technology 2024YFE0102700, 2023YFA0914303, Shenzhen Science and Technology Innovation Commission WDZC20220811144737001, the Jilin Fuyuan Guan Food Group Co., Ltd, startup fund OD2021031C, Interdisciplinary Research and Innovation Fund JC2022008, Overseas Research Cooperation Fund HW2024009 from Tsinghua SIGS (to T.T.),

Author contributions

X.G. and T.T. conceived and designed the project. X.G. and X.Q. performed wet experiments and analyzed image data. X.G. and D.S. performed image quantification and computational analysis. X.G. and T.T. wrote the manuscript.

Competing interests

The authors declare no competing interests.

References

1. van Bergeijk, P., Hoogenraad, C.C., and Kapitein, L.C. (2016). Right Time, Right Place: Probing the Functions of Organelle Positioning. Trends Cell Biol *26*, 121–134. https://doi.org/10.1016/j.tcb.2015.10.001.

2. Teti, A. (1992). Regulation of cellular functions by extracellular matrix. Journal of the American Society of Nephrology *2*, S83. https://doi.org/10.1681/ASN.V210s83.

3. Luo, Y., Na, Z., and Slavoff, S.A. (2018). P-Bodies: Composition, Properties, and Functions. Biochemistry *57*, 2424–2431. https://doi.org/10.1021/acs.biochem.7b01162.

4. West, A.P., and Shadel, G.S. (2017). Mitochondrial DNA in innate immune responses and inflammatory pathology. Nat Rev Immunol *17*, 363–375. https://doi.org/10.1038/nri.2017.21.

5. Ow, Y.-L.P., Green, D.R., Hao, Z., and Mak, T.W. (2008). Cytochrome c: functions beyond respiration. Nat Rev Mol Cell Biol *9*, 532–542. https://doi.org/10.1038/nrm2434.

6. Wang, B., Zhang, L., Dai, T., Qin, Z., Lu, H., Zhang, L., and Zhou, F. (2021). Liquid–liquid phase separation in human health and diseases. Signal Transduct Target Ther *6*, 290. https://doi.org/10.1038/s41392-021-00678-1.

7. Choi, Y.-J., and Song, K. (2022). Nst1, Densely Associated to P-Body in the Post-Exponential Phases of Saccharomyces cerevisiae, Shows an Intrinsic Potential of Producing Liquid-Like Condensates of P-Body Components in Cells. Int J Mol Sci *23*, 2501. https://doi.org/10.3390/ijms23052501.

8. Noda, N.N., Wang, Z., and Zhang, H. (2020). Liquid–liquid phase separation in autophagy. Journal of Cell Biology *219*. https://doi.org/10.1083/jcb.202004062.

9. Parker, R., and Sheth, U. (2007). P Bodies and the Control of mRNA Translation and Degradation. Mol Cell *25*, 635–646. https://doi.org/10.1016/j.molcel.2007.02.011.

10. Eulalio, A., Behm-Ansmant, I., and Izaurralde, E. (2007). P bodies: at the crossroads of post-transcriptional pathways. Nat Rev Mol Cell Biol *8*, 9–22. https://doi.org/10.1038/nrm2080.

11. Decker, C.J., and Parker, R. (2012). P-Bodies and Stress Granules: Possible Roles in the Control of Translation and mRNA Degradation. Cold Spring Harb Perspect Biol *4*, a012286–a012286. https://doi.org/10.1101/cshperspect.a012286.

12. Decker, C.J., Teixeira, D., and Parker, R. (2007). Edc3p and a glutamine/asparagine-rich domain of Lsm4p function in processing body assembly in *Saccharomyces cerevisiae*. J Cell Biol *179*, 437–449. https://doi.org/10.1083/jcb.200704147.

13. Xing, W., Muhlrad, D., Parker, R., and Rosen, M.K. (2020). A quantitative inventory of yeast P body proteins reveals principles of composition and specificity. Elife *9*. https://doi.org/10.7554/eLife.56525.

14. van Dijk, E. (2002). Human Dcp2: a catalytically active mRNA decapping enzyme located in specific cytoplasmic structures. EMBO J *21*, 6915–6924. https://doi.org/10.1093/emboj/cdf678.

15. Hurto, R.L., and Hopper, A.K. (2011). P-body components, Dhh1 and Pat1, are involved in tRNA nuclear-cytoplasmic dynamics. RNA *17*, 912–924. https://doi.org/10.1261/rna.2558511.

482 16. Sachdev, R., Hondele, M., Linsenmeier, M., Vallotton, P., Mugler, C.F., Arosio, P., and Weis, K.
483 (2019). Pat1 promotes processing body assembly by enhancing the phase separation of the DEAD-
484 box ATPase Dhh1 and RNA. Elife *8*. https://doi.org/10.7554/eLife.41415.

485 17. INGELFINGER, D., ARNDT-JOVIN, D.J., LÜHRMANN, R., and ACHSEL, T. (2002). The
486 human LSm1-7 proteins colocalize with the mRNA-degrading enzymes Dcp1/2 and Xrn1 in
487 distinct cytoplasmic foci. RNA *8*, 1489–1501. https://doi.org/10.1017/S1355838202021726.

488 18. Rao, B.S., and Parker, R. (2017). Numerous interactions act redundantly to assemble a tunable size
489 of P bodies in *Saccharomyces cerevisiae*. Proceedings of the National Academy of Sciences *114*.
490 https://doi.org/10.1073/pnas.1712396114.

491 19. Teixeira, D., and Parker, R. (2007). Analysis of P-Body Assembly in *Saccharomyces cerevisiae*.
492 Mol Biol Cell *18*, 2274–2287. https://doi.org/10.1091/mbc.e07-03-0199.

493 20. Shimobayashi, S.F., Ronceray, P., Sanders, D.W., Haataja, M.P., and Brangwynne, C.P. (2021).
494 Nucleation landscape of biomolecular condensates. Nature *599*. https://doi.org/10.1038/s41586-
495 021-03905-5.

496 21. Shin, Y., Chang, Y.C., Lee, D.S.W., Berry, J., Sanders, D.W., Ronceray, P., Wingreen, N.S.,
497 Haataja, M., and Brangwynne, C.P. (2018). Liquid Nuclear Condensates Mechanically Sense and
498 Restructure the Genome. Cell *175*. https://doi.org/10.1016/j.cell.2018.10.057.

499 22. Lee, D.S.W., Choi, C.H., Sanders, D.W., Beckers, L., Riback, J.A., Brangwynne, C.P., and
500 Wingreen, N.S. (2023). Size distributions of intracellular condensates reflect competition between
501 coalescence and nucleation. Nat Phys *19*. https://doi.org/10.1038/s41567-022-01917-0.

502 23. Espinosa, J.R., Joseph, J.A., Sanchez-Burgos, I., Garaizar, A., Frenkel, D., and Collepardo-
503 Guevara, R. (2020). Liquid network connectivity regulates the stability and composition of
504 biomolecular condensates with many components. Proc Natl Acad Sci U S A *117*.
505 https://doi.org/10.1073/pnas.1917569117.

506 24. Schmoller, K.M., and Skotheim, J.M. (2015). The Biosynthetic Basis of Cell Size Control. Trends
507 Cell Biol *25*, 793–802. https://doi.org/10.1016/j.tcb.2015.10.006.

508 25. Goehring, N.W., and Hyman, A.A. (2012). Organelle Growth Control through Limiting Pools of
509 Cytoplasmic Components. Current Biology *22*, R330–R339.
510 https://doi.org/10.1016/j.cub.2012.03.046.

511 26. Chan, Y.-H.M., and Marshall, W.F. (2010). Scaling properties of cell and organelle size.
512 Organogenesis *6*, 88–96. https://doi.org/10.4161/org.6.2.11464.

513 27. Chan, Y.-H.M., and Marshall, W.F. (2014). Organelle Size Scaling of the Budding Yeast Vacuole
514 Is Tuned by Membrane Trafficking Rates. Biophys J *106*, 1986–1996.
515 https://doi.org/10.1016/j.bpj.2014.03.014.

516 28. Rafelski, S.M., Viana, M.P., Zhang, Y., Chan, Y.-H.M., Thorn, K.S., Yam, P., Fung, J.C., Li, H.,
517 Costa, L. da F., and Marshall, W.F. (2012). Mitochondrial Network Size Scaling in Budding
518 Yeast. Science (1979) *338*, 822–824. https://doi.org/10.1126/science.1225720.

519 29. Jorgensen, P., Edgington, N.P., Schneider, B.L., Rupeš, I., Tyers, M., and Futcher, B. (2007). The
520 Size of the Nucleus Increases as Yeast Cells Grow. Mol Biol Cell *18*, 3523–3532.
521 https://doi.org/10.1091/mbc.e06-10-0973.

522 30. Lanz, M.C., Zhang, S., Swaffer, M.P., Ziv, I., Götz, L.H., Kim, J., McCarthy, F., Jarosz, D.F.,
523 Elias, J.E., and Skotheim, J.M. (2024). Genome dilution by cell growth drives starvation-like
524 proteome remodeling in mammalian and yeast cells. Nat Struct Mol Biol *31*, 1859–1871.
525 https://doi.org/10.1038/s41594-024-01353-z.

526 31. Zhurinsky, J., Leonhard, K., Watt, S., Marguerat, S., Bähler, J., and Nurse, P. (2010). A
527 Coordinated Global Control over Cellular Transcription. Current Biology *20*, 2010–2015.
528 https://doi.org/10.1016/j.cub.2010.10.002.

529 32. Newman, J.R.S., Ghaemmaghami, S., Ihmels, J., Breslow, D.K., Noble, M., DeRisi, J.L., and
530 Weissman, J.S. (2006). Single-cell proteomic analysis of S. cerevisiae reveals the architecture of
531 biological noise. Nature *441*, 840–846. https://doi.org/10.1038/nature04785.

532 33. Safieddine, A., Benassy, M.-N., Bonte, T., Slimani, F., Pourcelot, O., Kress, M., Ernoult-Lange,
533 M., Courel, M., Coleno, E., Imbert, A., et al. (2024). Cell-cycle-dependent mRNA localization in
534 P-bodies. Mol Cell *84*, 4191-4208.e7. https://doi.org/10.1016/j.molcel.2024.09.011.

535 34. Harvey, S.L., Enciso, G., Dephoure, N., Gygi, S.P., Gunawardena, J., and Kellogg, D.R. (2011). A
536 phosphatase threshold sets the level of Cdk1 activity in early mitosis in budding yeast. Mol Biol
537 Cell *22*, 3595–3608. https://doi.org/10.1091/mbc.e11-04-0340.

538 35. Jorgensen, P., Nishikawa, J.L., Breitkreutz, B.-J., and Tyers, M. (2002). Systematic Identification
539 of Pathways That Couple Cell Growth and Division in Yeast. Science (1979) *297*, 395–400.
540 https://doi.org/10.1126/science.1070850.

541 36. Li, Y., Jiang, Y., Paxman, J., O'Laughlin, R., Klepin, S., Zhu, Y., Pillus, L., Tsimring, L.S., Hasty,
542 J., and Hao, N. (2020). A programmable fate decision landscape underlies single-cell aging in
543 yeast. Science (1979) *369*, 325–329. https://doi.org/10.1126/SCIENCE.AAX9552.

544 37. Zhou, Z., Liu, Y., Feng, Y., Klepin, S., Tsimring, L.S., Pillus, L., Hasty, J., and Hao, N. (2023).
545 Engineering longevity - design of a synthetic gene oscillator to slow cellular aging. Science (1979)
546 *380*. https://doi.org/10.1126/science.add7631.

547 38. Lambert, G.G., Depernet, H., Gotthard, G., Schultz, D.T., Navizet, I., Lambert, T., Adams, S.R.,
548 Torreblanca-Zanca, A., Chu, M., Bindels, D.S., et al. (2020). Aequorea's secrets revealed: New
549 fluorescent proteins with unique properties for bioimaging and biosensing. PLoS Biol *18*,
550 e3000936. https://doi.org/10.1371/journal.pbio.3000936.

551 39. Tsuboi, T., Viana, M.P., Xu, F., Yu, J., Chanchani, R., Arceo, X.G., Tutucci, E., Choi, J., Chen,
552 Y.S., Singer, R.H., et al. (2020). Mitochondrial volume fraction and translation duration impact
553 mitochondrial mRNA localization and protein synthesis. Elife *9*.
554 https://doi.org/10.7554/eLife.57814.

555 40. Ostwald ripening (2014). In The IUPAC Compendium of Chemical Terminology (International
556 Union of Pure and Applied Chemistry (IUPAC)). https://doi.org/10.1351/goldbook.O04348.

557 41. Xing, W., Muhlrad, D., Parker, R., and Rosen, M.K. (2020). A quantitative inventory of yeast P
558 body proteins reveals principles of composition and specificity. Elife *9*.
559 https://doi.org/10.7554/eLife.56525.

560 42. Lee, S., Lim, W.A., and Thorn, K.S. (2013). Improved Blue, Green, and Red Fluorescent Protein
561 Tagging Vectors for S. cerevisiae. PLoS One *8*, e67902.
562 https://doi.org/10.1371/journal.pone.0067902.

563 43. Li, Y., Jiang, Y., Paxman, J., O'laughlin, R., Klepin, S., Zhu, Y., Pillus, L., Tsimring, L.S., Hasty,
564 J., and Hao, N. A programmable fate decision landscape underlies single-cell aging in yeast.

565 44. Paxman, J., Zhou, Z., O'Laughlin, R., Liu, Y., Li, Y., Tian, W., Su, H., Jiang, Y., Holness, S.E.,
566 Stasiowski, E., et al. (2022). Age-dependent aggregation of ribosomal RNA-binding proteins links
567 deterioration in chromatin stability with challenges to proteostasis. Elife *11*.
568 https://doi.org/10.7554/eLife.75978.

569 45. Joyner, R.P., Tang, J.H., Helenius, J., Dultz, E., Brune, C., Holt, L.J., Huet, S., Müller, D.J., and
570 Weis, K. (2016). A glucose-starvation response regulates the diffusion of macromolecules. Elife *5*.
571 https://doi.org/10.7554/eLife.09376.

572

573

574

575

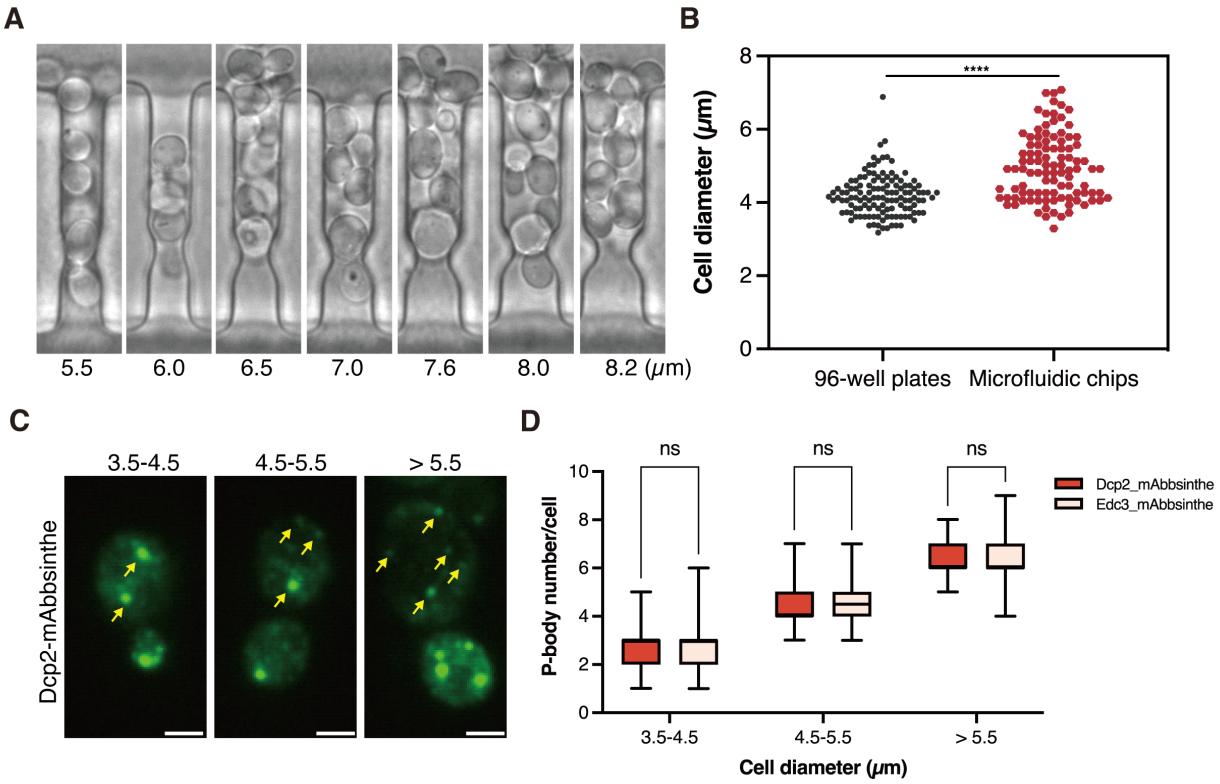

Figure 1 | P-bodies number increases with increasing yeast cell size

(A) Different sizes of the cells are captured in the microfluidic device based on the well size written below.

(B) The size of the cells in 96-well plates and microfluidic chips. Each dot corresponds to one cell (n>90). Statistical significance was assessed by the Unpaired T-test (**** $P < 0.0001$).

(C) P-bodies in varying sizes of yeast cells were labeled with Dcp2_mAbbsinthe and analyzed 30 minutes after glucose starvation. Yellow arrows indicate P-bodies in mother cells. Scale bar, 2 μm.

(D) P-body number per cell across different cell sizes. Yeast cells expressing Dcp2_mAbbsinthe or Edc3_mAbbsinthe were categorized into three size ranges based on cell diameter. Statistical significance was assessed by Unpaired T-test (ns $P > 0.05$, n>30).

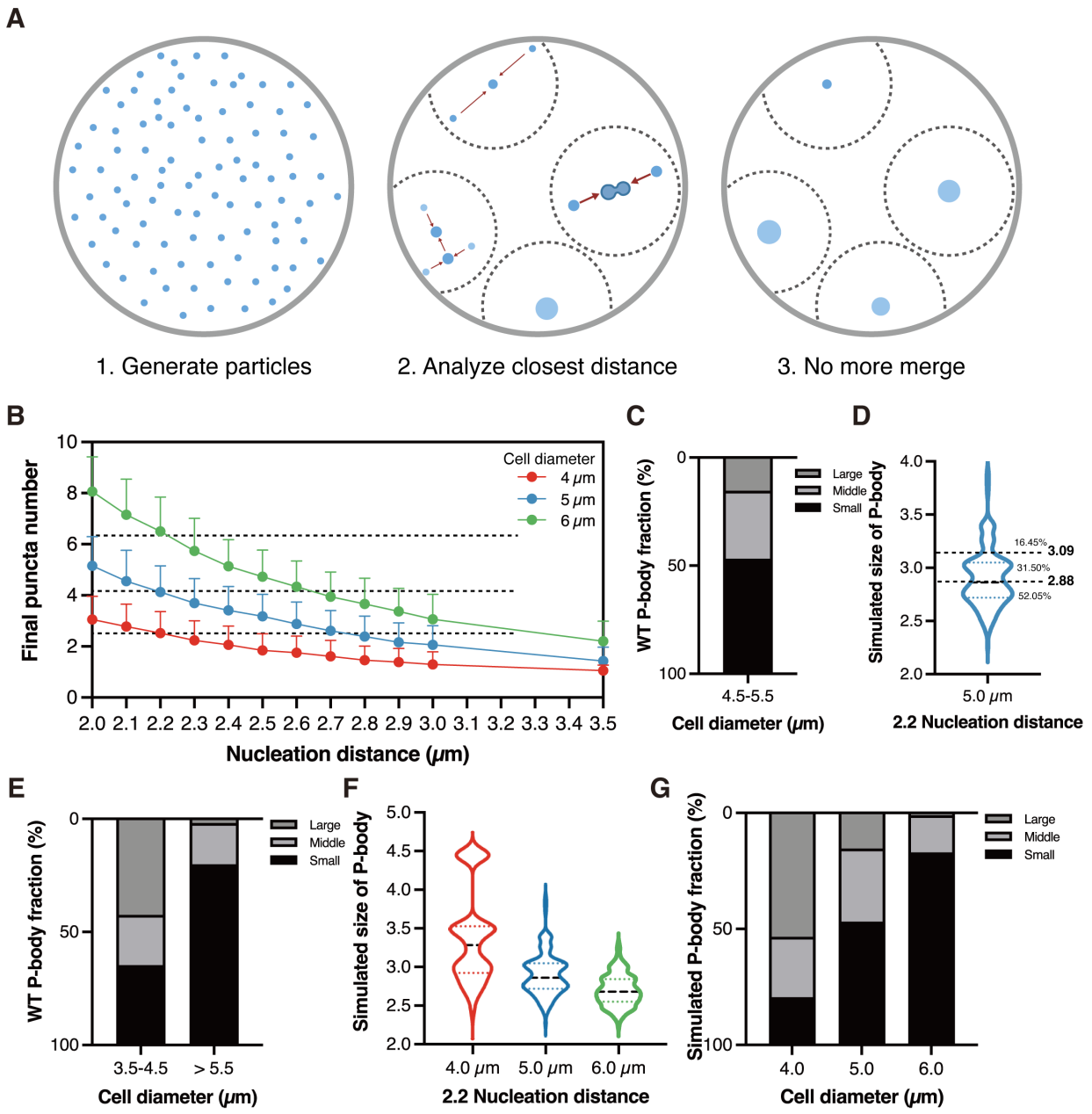

Figure 2 | A Monte-Carlo simulation based on nucleation identifies a characteristic nucleation distance

(A) Particle nucleation model based on Monte Carlo simulation. 1. Generate particles: Initial distribution of molecules in 3D space before simulation, each blue dot represents a molecule. 2. Analyze the closest distance: Each molecule recognizes the closest one and then fuses. 3. No more

merge: Result of the merge model simulation, showing puncta left after fusion, each granule represents a P-body.

(B) Nucleation distance correlates with the final puncta number. Based on the nucleation distance, final puncta numbers were simulated for each cell size. (n = 200 per condition). Horizontal dashed lines indicate the mean P-body number per cell of different cell size groups in Figure 1D.

(C) Size fraction of P-body in the 4.5-5.5μm cell size by the manual classification of microscope image.

(D) The definition of the simulated size of the P-body. The boundary for different sizes of P-bodies in the simulation is based on the fraction in C.

(E) Size fraction of P-body in the different cell sizes by the manual classification of microscope image data.

(F) Size of P-bodies in different cell sizes at the d_n = 2.2 μm in the simulation.

(G) Fractions of the simulated P-body size in the different cell sizes based on the definition in D.

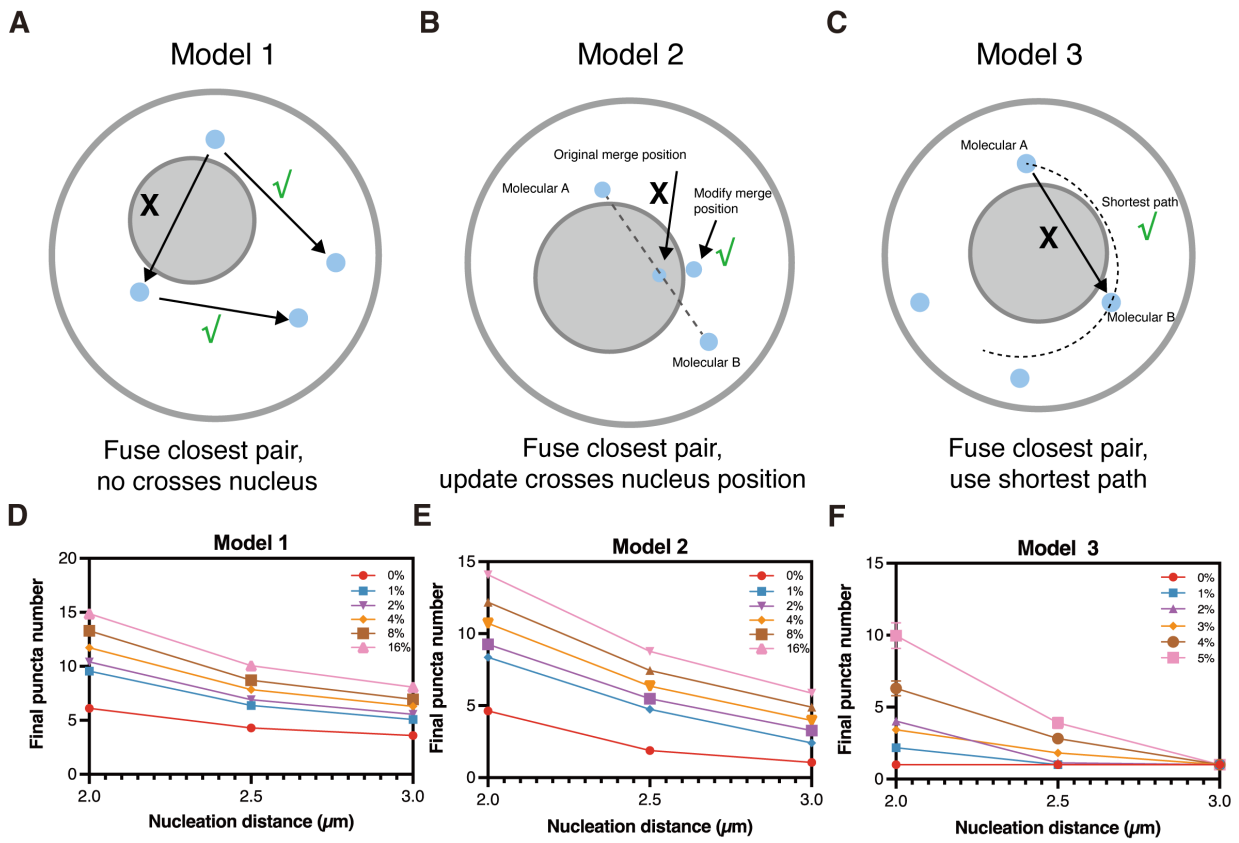

Figure 3 | Organelle occupancy amplifies nucleation frequency by restricting effective cytoplasmic volume

(A-C) Schematic diagrams of three different molecular nucleation models in a cell with a central occupation by an organelle (gray circle).

(A) Model 1: Molecules fuse with their closest neighbor only if the connecting line does not intersect the central organelle.

(B) Model 2: Molecules fuse with their closest neighbor even if the direct path crosses the nucleus, but the merged granule is repositioned to avoid overlap with the central organelle.

(C) Model 3: Molecules fuse with their closest neighbor based on the true shortest path around the nucleus, allowing nucleus-aware trajectories.

619 (D-F) The final puncta number under different nucleation distances and varying organelle
620 fractions. The color represents the different organelle fractions relative to the cell.
621

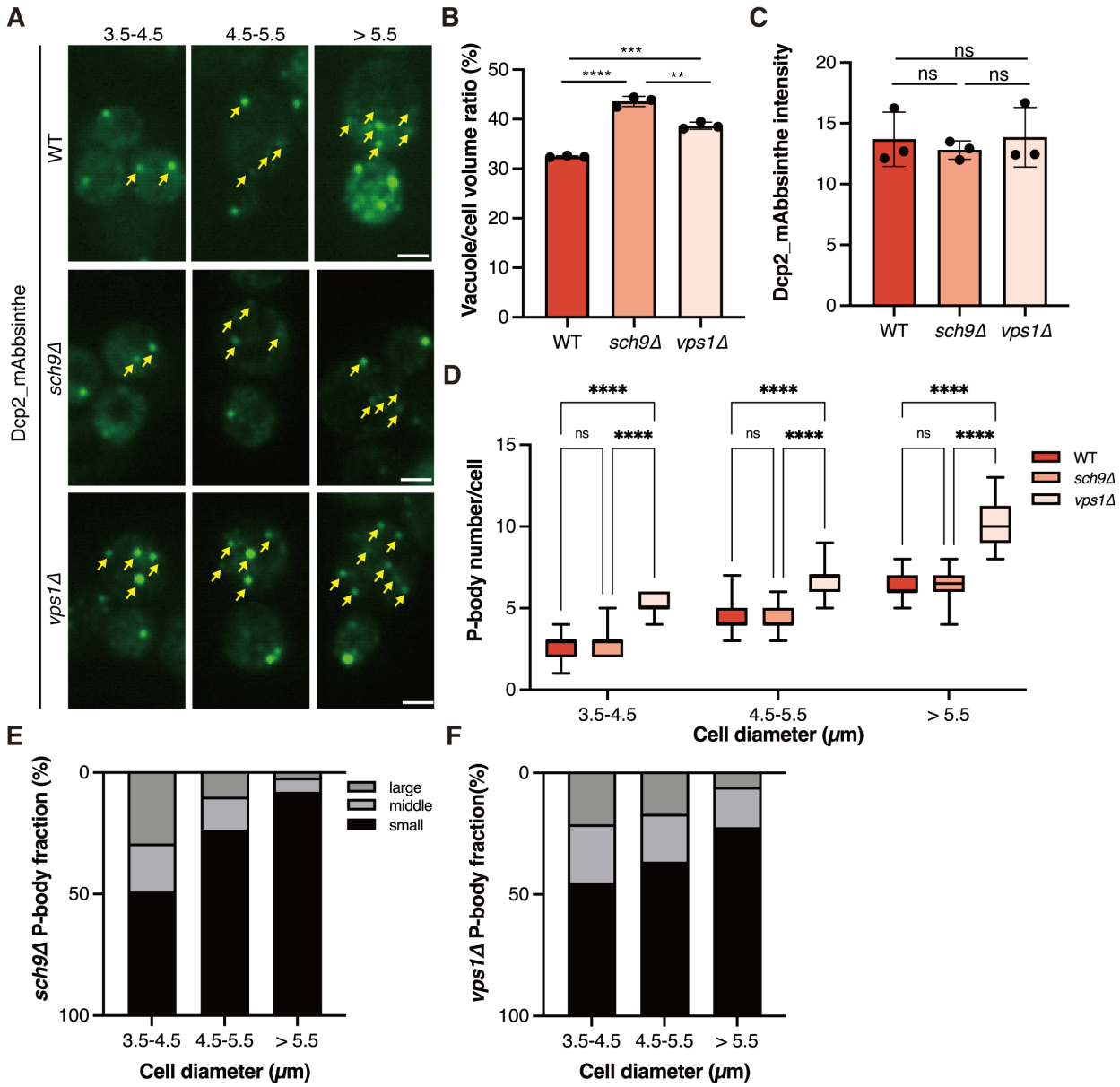

Figure 4 | Vacuole mutants validate the influence of spatial confinement on P-body assembly

(A) Visualization of P-bodies in WT, *sch9*Δ, and *vps1*Δ yeast strains expressing Dcp2_mAbbsinthe under glucose starvation for 30 minutes. Cells are grouped by cell diameter (3.5-4.5, 4.5-5.5, >5.5), and P-bodies are indicated by arrows. Images are z-projections of 42 slices. Scale bar, 2 µm.

628 (B) Quantification of vacuole-to-cell volume ratio in WT, *sch9*Δ, and *vps1*Δ strains. Each dot
629 represents an individual experiment (n = 3 biological replicates). Statistical analysis was performed
630 using one-way ANOVA with multiple comparisons (**P < 0.01, ***P < 0.001, ****P < 0.0001).
631 (C) Intensity of Dcp2_mAbbsinthe fluorescence in WT, *sch9*Δ, and *vps1*Δ strains. No significant
632 differences were observed. Each dot represents an individual experiment.
633 (D) P-body number per cell across different cell diameter groups (3.5-4.5 µm, 4.5-5.5 µm, >5.5
634 µm) in WT, *sch9*Δ, and *vps1*Δ strains. Statistical significance was determined by two-way
635 ANOVA with multiple comparisons (ns P > 0.05, ****P < 0.0001).
636 (E) Proportion of large, middle, and small P-bodies in *sch9*Δ cells across the cell size groups.
637 (F) Proportion of large, middle, and small P-bodies in *vps1*Δ cells across the cell size groups.
638

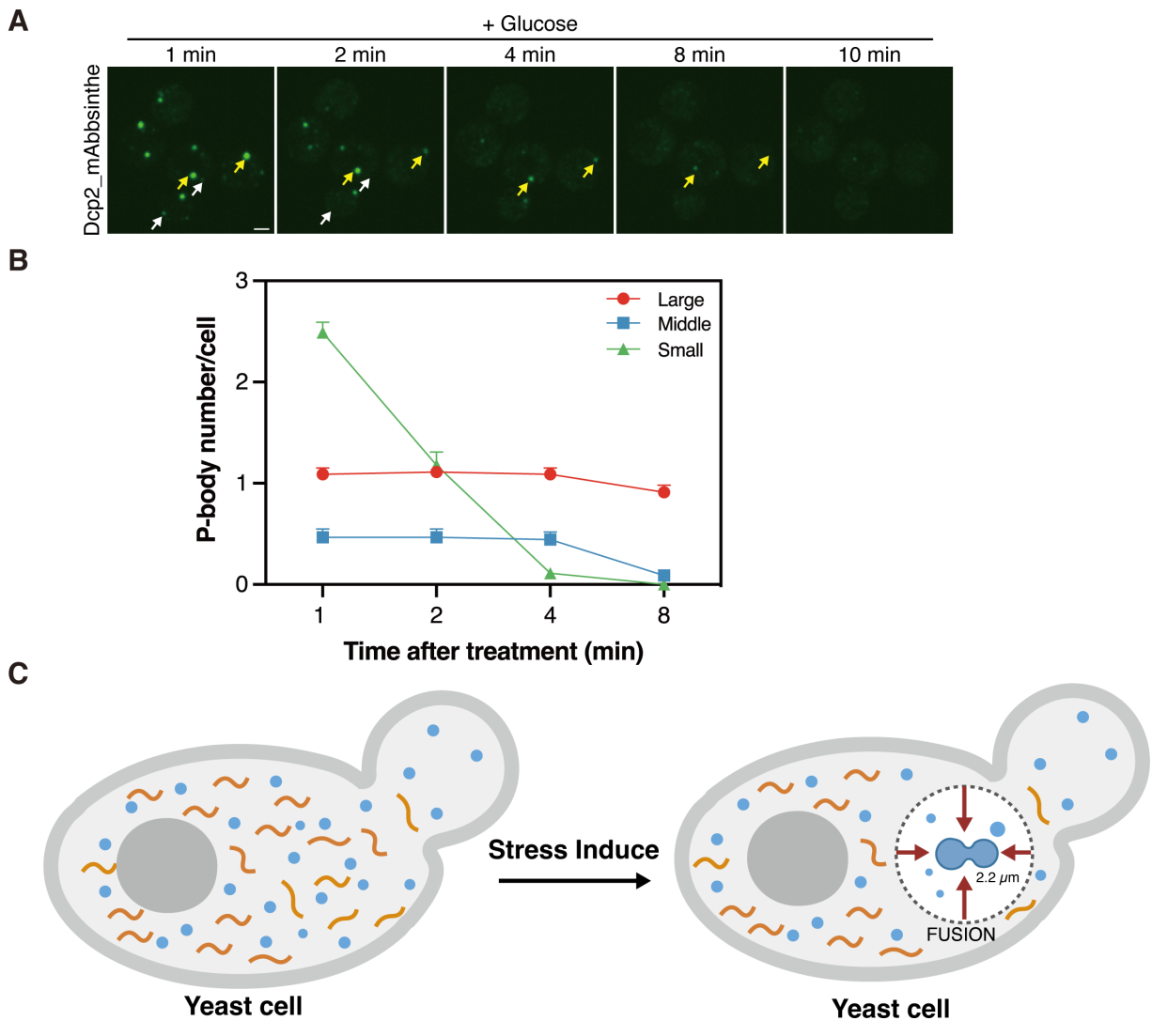

Figure 5 | Larger P-bodies exhibit delayed disassembly upon nutrient repletion

(A) Time-lapse images of P-bodies in yeast cells after glucose addition, following prior glucose starvation of 30 minutes. Images were taken at 1, 2, 4, 8, and 10 minutes after the addition of glucose. Yellow arrows indicate large P-bodies, white arrows indicate small P-bodies. Images are z-projections of 42 slices. Scale bar, 2 µm.

(B) Quantification of the number of P-bodies per cell over time after glucose addition. Small P-bodies rapidly disaggregate following glucose treatment, while large P-bodies are more stable. P-

647 body size is primarily determined at the initial time point of formation. n> 45 cells within three
648 independent experiments.
649 (C) A schematic model description of P-body formation in yeast cells. Upon stress induction,
650 molecular components (blue dots) and mRNA (orange lines) condense into P-bodies via nucleation
651 within a spatial nucleation distance (~2.2 μm).
652

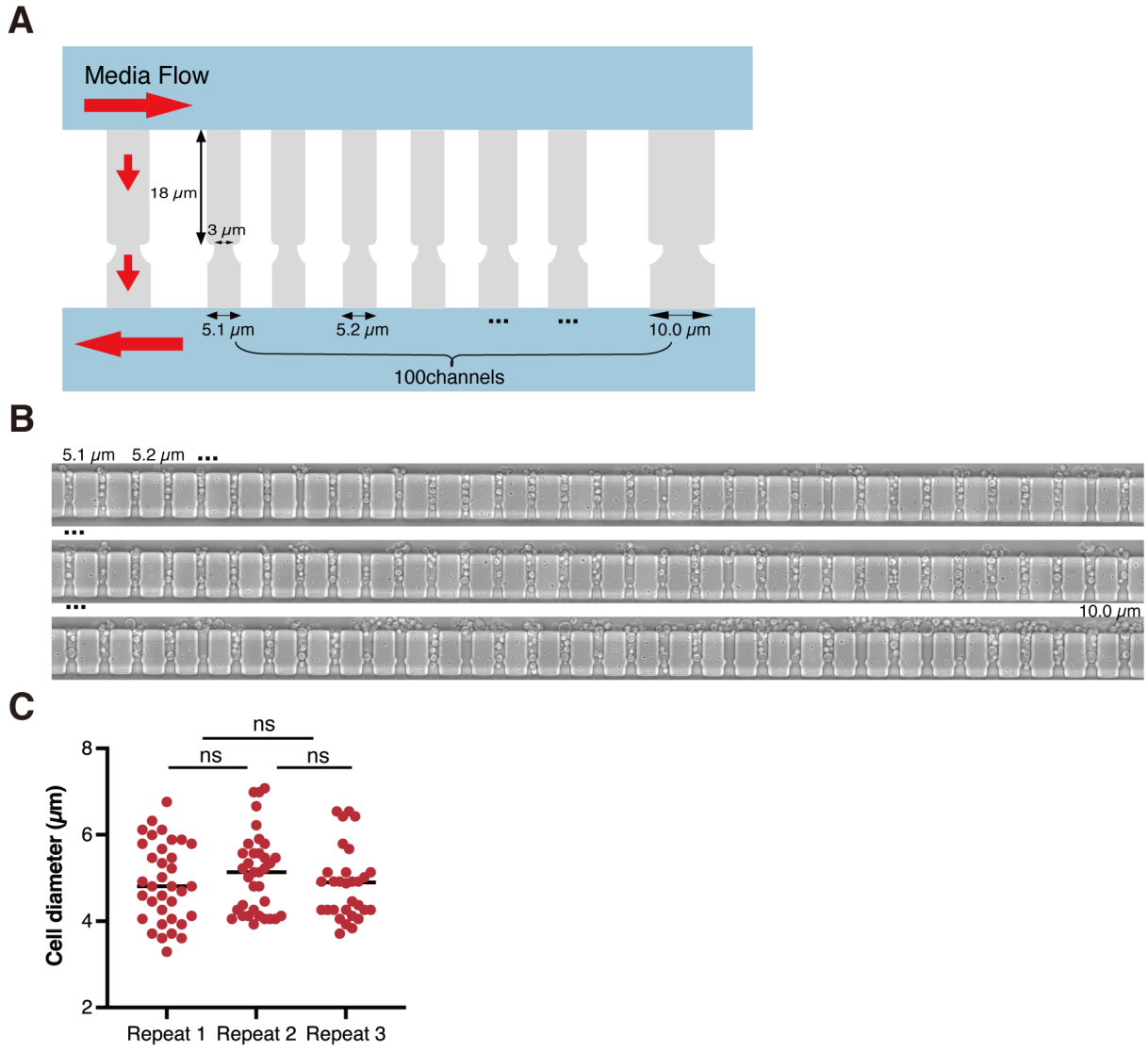

Supplementary Figure 1 | Design of microfluidics for different sizes of the cells

(A) Design of microfluidics for different sizes of the cells.

(B) Example of a microfluidic device with a well size of from 5.1 μm to 10 μm.

(C) The microfluidics can capture different size of the cells consistently (n ≥ 30 cells per repeat).

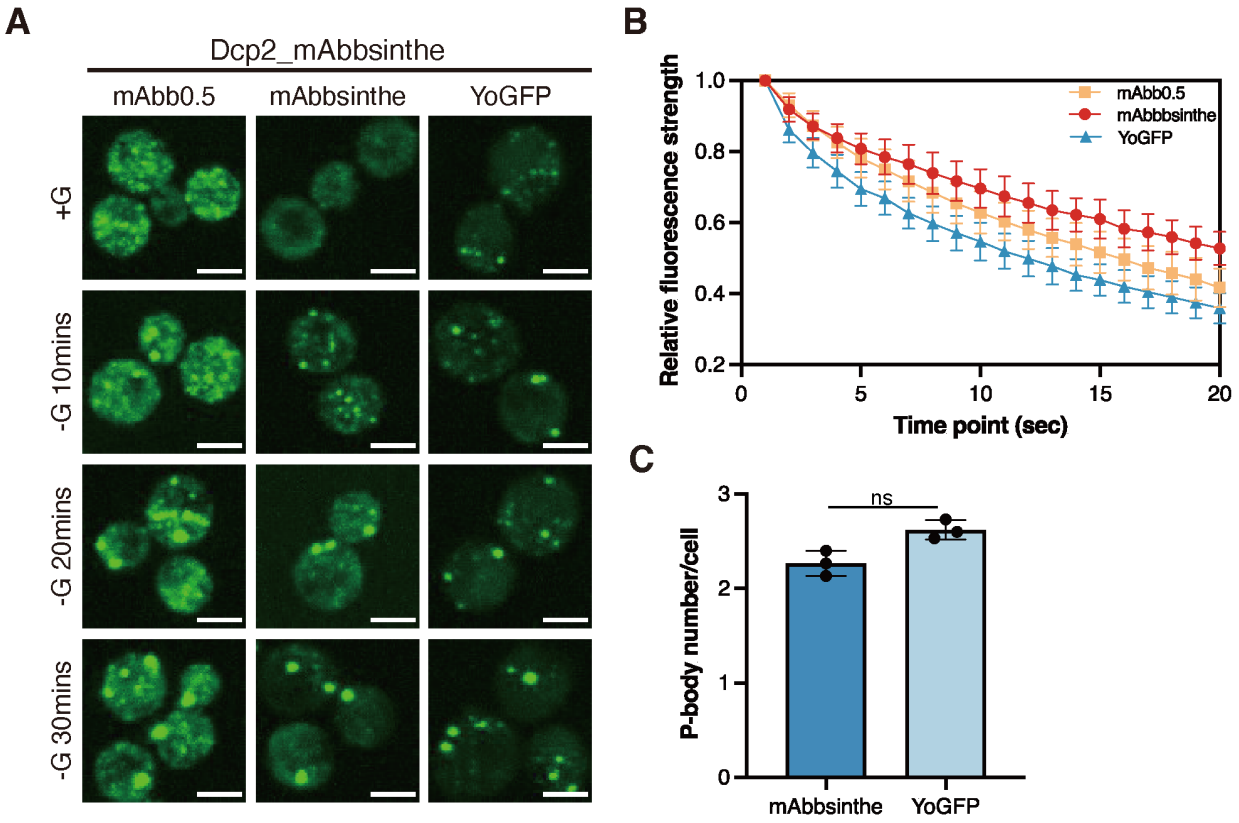

Supplementary Figure 2 | Dcp2 labeled with mAbbsinthe exhibits similar condensation and greater resistance to photobleaching compared to GFP

(A) Z-stack images of Dcp2 labeled with mAbb0.5, mAbbsinthe, and YoGFP. Cells were visualized upon glucose (G) starvation for 0, 10, 20, and 30 minutes. The scale bar indicates 2 µm.

(B) Various Dcp2-GFPs were photobleached under a 10-Watt laser for a 50-ms exposure for each time point. The fluorescence recovery was monitored over 20 seconds (n = 30 cells), and the relative fluorescence strength was plotted.

(C) Number of P-bodies per cell for mAbbsinthe and YoGFP-tagged Dcp2 under glucose starvation for 30 min. Statistical significance was assessed by the Unpaired T-test (ns $P > 0.05$, $n>30$).

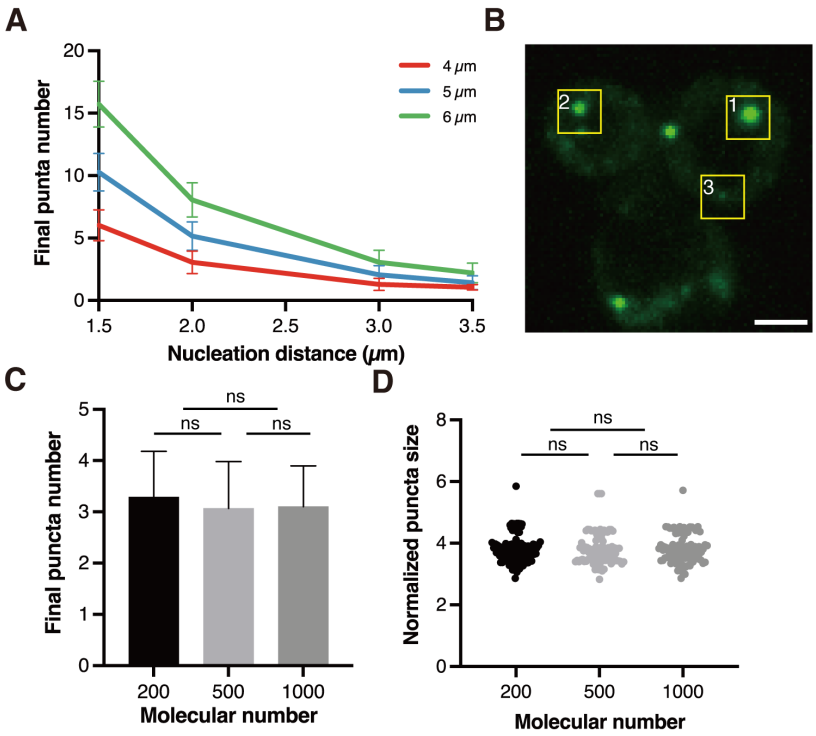

Supplementary Figure 3 | Effects of nucleation distance and molecular number on P-body formation simulation.

(A) Relationship between the final puncta number across different nucleation distances with different sizes of the cell.

(B) Example of the different P-body sizes. Yellow boxes highlight the representative P-bodies in the different size groups. 1 - large, 2 - middle, and 3 - small groups, respectively.

(C) The final puncta number is independent of molecular concentration in the nucleation simulation. Bar graph shows the final number of simulated P-bodies when varying the initial number of molecules (200, 500, 1000). Statistical significance was assessed by the Unpaired T-test (ns $P > 0.05$, $n = 200$ simulations per group).

(D) Punta size distribution does not change upon molecular number.